Effective diahaline diffusivities in estuaries

Hans Burchard*, Ulf Gräwe, Knut Klingbeil, Nicky Koganti, Xaver Lange, Marvin Lorenz

Leibniz Institute for Baltic Sea Research Warnemünde, Rostock, Germany

**Corresponding author address:* Hans Burchard, Leibniz Institute for Baltic Sea Research Warnemünde, Seestraße 15, D-18119 Rostock, Germany.

E-mail: hans.burchard@io-warnemuende.de

ABSTRACT

The aim of the present study is to estimate effective diahaline turbulent salinity fluxes and diffusivities in numerical model simulations of estuarine scenarios. The underlying method is based on a quantification of salinity mixing per salinity class, which is shown to be twice the turbulent salinity transport across the respective isohaline. Using this relation, the recently derived universal law of estuarine mixing, predicting that average mixing per salinity class is twice the respective salinity times the river run-off, can be directly derived. The turbulent salinity transport is accurately decomposed into physical (due to the turbulence closure) and numerical (due to truncation errors of the salinity advection scheme) contributions. The effective diahaline diffusivity representative for a salinity class and an estuarine region results as the ratio of the diahaline turbulent salinity transport and the respective (negative) salinity gradient, both integrated over the isohaline area in that region and averaged over a specified period. With this approach, the physical (or numerical) diffusivities are calculated as half of the product of physical (or numerical) mixing and the isohaline volume, divided by the square of the isohaline area. The method for accurately calculating physical and numerical diahaline diffusivities is tested and demonstrated for a three-dimensional idealized exponential estuary. As a major product of this study, maps of the spatial distribution of the effective diahaline diffusivities are shown for the model estuary.

1. Introduction

The circulation and hydrography of estuaries is largely determined by turbulent mixing. This has been impressively demonstrated by the laboratory experiments conducted by Linden and Simpson (1986), generating lock exchange flows under the impact of air bubble-induced turbulence. They could show that strong turbulence slowed down the exchange flow driven by gravitational forces and used this as an explanation for the tidal modulation of estuarine circulation (Linden and Simpson 1988). Earlier, using a simple analytical model, Hansen and Rattray (1965) quantified how the intensity of estuarine exchange flow is inversely proportional to specified constant vertical eddy viscosity and diffusivity. In an idealized numerical model study, Hetland and Geyer (2004) showed how the length of an estuary, i.e., the longitudinal extent of the brackish water zone, depends on a prescribed eddy viscosity and diffusivity: high eddy coefficients result in short estuaries and vice-versa. This process is reflected by observations and model results for many estuaries: During phases of high turbulence (spring tides), vertical stratification is reduced due to more upright isohaline surfaces, resulting in shorter estuaries and vice versa during low turbulence (neap tide), see e.g., Warner et al. (2005) for the Hudson River Estuary and Li et al. (2018) for the Changjiang River Estuary.

In contrast to local and instantaneous diffusivities as parameterized in ocean models by turbulence closures (see, e.g., Large et al. 1994; Umlauf and Burchard 2005), effective diffusivities are often calculated to analyze diffusive transport in water bodies of different characteristics. The latter are generally calculated as the (negative) ratio of turbulent flux and tracer gradient, both individually averaged over a surface (e.g., an isopycnal) and over time, such they result as weighted integral averages of the local and instantaneous diffusivities. The substantially inhomogeneous distribution of eddy diffusivity (low in the interior, high at sloping bottoms) has the consequence that effective diffusivities on various types of basins are easily an order of magnitude larger than the local ones observed in the interior, such as found, e.g., for the world ocean (Waterhouse et al. 2014), the Baltic Sea (Holtermann et al. 2012) or lakes (Goudsmit et al. 1997).

In ocean models, diffusivities are typically conterminated by numerical spurious mixing by tracer advection schemes, such that water mass transformations parameterized by carefully calibrated turbulence closure models might be overridden by numerical diffusion. Various methods have been proposed to estimate effective diffusivities in ocean models, either based on the increase of background potential energy (Griffies et al. 2000; Ilıcak et al. 2012), on numerical tracer releases (Getzlaff et al. 2010, 2012) or on water mass transformation analysis evaluating overturning streamfunctions (Lee et al. 2002; Megann 2018). All these methods share the drawback that the analysis averages effective diffusivities over large regions. Methods for locally analyzing physical and numerical mixing based on decay of tracer variance have been proposed by Burchard and Rennau (2008) and Klingbeil et al. (2014). These methods however do not yet allow computing diapycnal diffusivities.

In estuaries, effective longitudinal diffusivities, i.e., the ratio of longitudinal turbulent salinity fluxes and salinity gradients individually averaged over vertical transects, are several orders of magnitude larger than vertical diffusivities (Fischer 1976). This is mainly due to the process of shear dispersion (Taylor 1954; Young and Jones 1991), a combination of vertical diffusion and vertical shear. In order to reproduce salt intrusion, vertically or cross-sectionally integrated estuarine models which do not resolve tidal shear dispersion do therefore need to parameterize this process by means of large values of longitudinal diffusivity (Uncles and Stephens 1990; Ralston et al. 2008).

In early coastal ocean models, horizontal diffusivity was applied to suppress numerically induced oscillations (Blumberg and Mellor 1987). Recent models use monotone advection schemes including implicit numerical diffusion, such that explicit horizontal diffusion is not needed (see, e.g., Hofmeister et al. 2011; Ralston et al. 2017). The numerical mixing caused by these advection schemes as well as the physical mixing due to the turbulence closure model can be quantified as local and instantaneous dissipation of salinity variance (Burchard and Rennau 2008; Klingbeil et al. 2014). In some estuarine model simulations, the numerical mixing can account for a substantial part of the total mixing, such that a re-tuning of the turbulence closure is required to obtain satisfactory salinity distributions (Ralston et al. 2017).

In estuaries, density is largely determined by salinity, although for low-inflow estuaries, specifically in summer, also temperature might contribute to density stratification (Largier et al. 1996). Therefore, for typical strong-inflow estuaries, temperature variations are often neglected when analyzing the dynamics, with the consequence that isohaline and isopycnal surfaces are assumed to be identical. In recent years, one focus of estuarine physical studies has been the analysis of salinity mixing, defined as the decay of salinity variance (Burchard and Rennau 2008; Burchard et al. 2009). Based on the Total Exchange Flow (TEF) analysis framework introduced by MacCready (2011), the relation between the exchange flow and integrated estuarine salinity mixing of riverine fresh water and oceanic salt water was studied by several authors (Wang et al. 2017; MacCready et al. 2018; Burchard et al. 2019). To better understand estuarine dynamics, analysis of water mass transformations on isohaline surfaces (Walin 1977; MacCready and Geyer 2001; MacCready et al. 2002; Hetland 2005) is often advantageous over an analysis in geographical coordinates, since it is not conterminated by adiabatic (advective) processes such as tidal oscillations. Using the definition of mixing per salinity class (Wang et al. 2017), i.e., mixing integrated over infinitesimal isohaline volumes, Burchard (2020) could show that for long time integrations it converges towards twice the product of the respective salinity times the freshwater run-off. By using the analysis of physical and numerical mixing introduced by Klingbeil et al. (2014), the total mixing per salinity class could be decomposed into physical and numerical contributions, where the latter could become negative at times when anti-diffusive advection schemes are applied.

Due to the pivotal role of eddy diffusivity in estuaries, the aim of the present study is to estimate diahaline turbulent salinity fluxes and diffusivities in an estuarine numerical model simulation. This will be achieved by exploiting the recent concept of mixing on isohaline surfaces.

2. Mathematical derivation

The aim of this section is to review and further derive the isohaline framework within which the diahaline turbulent transport and the effective diahaline diffusivities are defined. The basic definitions of instantaneous mixing, fluxes and diffusivities are given in Sec. 2a. The isohaline geometry including isohaline surfaces and volumes is introduced in Sec. 2b. Based on this, diahaline mixing, transport and diffusivities are defined in Sec. 2c. Finally, in Sec. 2d, diahaline mixing relations and effective diahaline diffusivities for long-term averaged estuarine states are discussed in the light of these new results.

a. Salinity mixing and diahaline diffusivity

The basic physical equations from which the present theory is derived are the continuity equation (volume conservation, assuming incompressibility of sea water),

$$\vec{\nabla} \cdot \vec{u} = 0, \tag{1}$$

and the salinity equation (salt conservation),

$$\partial_t s + \vec{\nabla} \cdot (\vec{u} s) + \vec{\nabla} \cdot \vec{\mathscr{F}}^s_{\mathrm{diff}} = 0, \tag{2}$$

where $\vec{u}$ is the velocity vector, s is absolute salinity, and $\vec{\mathscr{F}}^s_{\mathrm{diff}} = (-K_h\partial_x s, -K_h\partial_y s, -K_v\partial_z s)$ is the turbulent (diffusive) salinity flux vector in Cartesian coordinates, where K_h and K_v are horizontal and vertical eddy diffusivities, respectively.

The salinity mixing per unit volume, χ, is defined as the local loss of salinity variance (Burchard and Rennau 2008),

$$\chi = -2\vec{\mathscr{F}}^s_{\mathrm{diff}} \cdot \vec{\nabla} s = 2K_h(\partial_x s)^2 + 2K_h(\partial_y s)^2 + 2K_v(\partial_z s)^2. \tag{3}$$

It should be noted that the single components of the turbulent salinity flux vector are down-gradient, but due to the non-isotropic eddy diffusivity ($K_h \gg K_v$) the entire vector itself is generally not down-gradient, and thus not orthogonal to the isohaline surface, see Fig. 1 and the discussion below.

In ocean models, the horizontal turbulent fluxes are typically aligned with the vertical model coordinate, e.g., with constant z-levels for geopotential models, constant σ-levels for models with σ-coordinates or constant density for isopycnal models. The vertical component of the turbulent fluxes is oriented either orthogonal to geopotential surfaces or orthogonal to isopycnal surfaces. Since typically isopycnal surfaces are rather flat, the difference between the latter two is generally negligible. In non-isopycnal models, the rotation of horizontal turbulent fluxes into isopycnal direction causes numerical problems (Griffies et al. 1998; Beckers et al. 1998) and is therefore sometimes avoided.

For any isohaline surface, we define the total (advective plus diffusive) diahaline salinity flux as

$$f^s = f^s_{\mathrm{adv}} + f^s_{\mathrm{diff}} = u_n s - K_n \partial_n s, \tag{4}$$

where $u_n = \vec{u} \cdot \vec{n}$ is the outgoing velocity with the normal vector $\vec{n} = \vec{\nabla} s / \left|\vec{\nabla} s\right|$ (pointing towards higher salinity), $\partial_n s = \vec{\nabla} s \cdot \vec{n}$ denotes the salinity gradient normal to the isohaline surface, and K_n is the diahaline diffusivity. Note that the diahaline turbulent salinity flux, $f^s_{\mathrm{diff}} = \vec{\mathscr{F}}^s_{\mathrm{diff}} \cdot \vec{n}$, is the orthogonal projection of the turbulent salinity flux vector to the isohaline surface, see Fig. 1 for an illustration. The definition (3) of the mixing per unit volume and the definition (4) of the diahaline turbulent salinity flux both imply an alternative expression for the diahaline diffusivity,

$$K_n = -\frac{f^s_{\mathrm{diff}}}{\partial_n s} = \frac{K_h(\partial_x s)^2 + K_h(\partial_y s)^2 + K_v(\partial_z s)^2}{(\partial_n s)^2} = \frac{\frac{1}{2}\chi}{(\partial_n s)^2}, \tag{5}$$

which means that the diahaline diffusivity depends on the salinity gradients. A consequence of this is that the diahaline diffusivities are different for each tracer although the horizontal and vertical diffusivities are not.

b. Isohaline volumes

We consider here a time-averaged estuarine volume $V(S)$ bounded in seaward direction by an isohaline of arbitrary salinity S with area $A(S)$, i.e., the volume contains estuarine water masses with a salinity s with $s \leq S$. The volume is further bounded by the air-sea interface at $z = \eta$ the river boundary area A_r located at zero salinity and zero salinity gradient, and the impermeable sea bottom at $z = -H$ (Fig. 2). The time-averaging operator is introduced for any function $X(t)$ as

$$\langle X \rangle (t) = \frac{1}{T} \int_{t-T/2}^{t+T/2} X(t')\,\mathrm{d}t', \tag{6}$$

where T is the averaging interval. Note, that for the limit of $T \to 0$, the non-averaged, instantaneous value $\langle X \rangle (t) = X(t)$ is obtained. In the following, we generally drop the argument t for time-averaged quantities. With this, $V(S)$ is formally defined as

$$V(S) = \left\langle \int_{V(S_{\max})} \mathscr{H}[S - s(x,y,z,t)]\,\mathrm{d}V \right\rangle, \tag{7}$$

with the heavyside function

$$\mathscr{H}[x] = \begin{cases} 0 & \text{for} \quad x < 0, \\ 1 & \text{for} \quad x \geq 0. \end{cases} \tag{8}$$

The isohaline volume had been defined by Walin (1977) as the infinitesimal volume per salinity class, for which different formulations can be used:

$$v(S) = \partial_S V(S) = \partial_S \int_0^S v(S')\,\mathrm{d}S' = \left\langle \int_{A(S)} (\partial_n s)^{-1}\,\mathrm{d}A \right\rangle, \tag{9}$$

where $(\partial_n s)^{-1}$ is the local and instantaneous infinitesimal thickness of the isohaline. Fig. 3 illustrates the definitions of volume per salinity class and thickness per salinity class by means of a finite salinity increment ΔS.

It should be noted that the isohaline volumes defined here depend on salinity S only. To retrieve information how these properties are distributed in horizontal space, the local thickness per salinity class, b^{loc}, and the accumulated local thickness with salinities $\leq S$, B^{loc}, can be defined as

$$b^{\mathrm{loc}}(S,x,y) = \partial_S B^{\mathrm{loc}}(S,x,y) \quad \text{with} \quad B^{\mathrm{loc}}(S,x,y) = \left\langle \int_{-H(x,y)}^{\eta(x,y,t)} \mathscr{H}[S - s(x,y,z,t)]\,\mathrm{d}z \right\rangle. \tag{10}$$

This allows for two different representations of the time-averaged isohaline depths.

We define the TEF-based mean isohaline surface height as

$$z^{\mathrm{TEF}}(S,x,y) = \langle \eta \rangle (x,y) - B^{\mathrm{loc}}(S,x,y). \tag{11}$$

The isohaline surface position can also be defined on the basis of the thickness-weighted time-averaged salinity distribution (obtained at constant σ levels, see Klingbeil et al. 2019), which is denoted as $z^{\mathrm{Eu}}(S,x,y)$ here. The isohaline height $z^{\mathrm{TEF}}(S)$ is motivated by the Total Exchange Flow (TEF) analysis framework proposed by MacCready (2011) and indicates an isohaline position inside the water column for all locations (x,y) where the salinity S has occurred during the averaging period for a finite period of time. In contrast, $z^{\mathrm{Eu}}(S)$ is the position of the isohaline S in the thickness-weighted salinity field.

For both representations, isohalines with salinities larger than all salinities in the water column are formally identical to the bottom coordinate and isohalines with salinities smaller than all salinities in the water column are formally identical to the mean surface position, $\langle \eta \rangle$. And for both, $z^{\mathrm{TEF}}(S,x,y)$ and $z^{\mathrm{Eu}}(S,x,y)$, isohaline volumes are identical. However, both representations of isohaline positions generally result in different isohaline areas, which will be denoted as $a^{\mathrm{TEF}}(S)$ and $a^{\mathrm{Eu}}(S)$, respectively. Generally, the TEF-based isohaline surface will be larger than the Eulerian mean one. With this, $b^{\mathrm{TEF}}(S) = v(S)/a^{\mathrm{TEF}}(S)$ and $b^{\mathrm{Eu}}(S) = v(S)/a^{\mathrm{Eu}}(S)$ are the area-averaged infinitesimal thicknesses per salinity class of the TEF-based and Eulerian mean salinity distributions, respectively. The area-averaged salinity gradients are then estimated as $\left(b^{\mathrm{TEF}}(S)\right)^{-1}$ and $\left(b^{\mathrm{Eu}}(S)\right)^{-1}$, respectively.

It should be noted that the calculations of the isohaline areas and the derived isohaline thicknesses are correct for the projections of the isohalines to geopotential surfaces. Increased areas and decreased thicknesses due to sloping isohalines are not taken into consideration. However, these errors are assumed to be small due to the small aspect ratio between vertical and horizontal scales in estuaries and the resulting small slopes of the isohalines. In numerical models, it is possible to correct for these errors, but for simplicity we refrain here to do so.

We consider the TEF-based representations of the isohaline structure as the physically sound one, since it indicates to which location in the (S,x,y)-space volume and other properties, such as mixing (see Sec. 2.c), are associated to. Therefore, from here onwards, the isohaline area is denoted as $a = a^{\mathrm{TEF}}(S)$ and the isohaline thickness as $b = b^{\mathrm{TEF}}(S)$.

c. Diahaline transport

The transport of volume and salinity through the isohaline surface is denoted as:

$$F^s(S) = \left\langle \int_{A(S)} f^s \,\mathrm{d}A \right\rangle, \quad F^s_{\mathrm{adv}}(S) = \left\langle \int_{A(S)} f_{\mathrm{adv}} s \,\mathrm{d}A \right\rangle, \quad F^s_{\mathrm{diff}}(S) = \left\langle \int_{A(S)} f^s_{\mathrm{diff}} \,\mathrm{d}A \right\rangle, \tag{12}$$

with the total salinity transport being denoted as $F^s = F^s_{\mathrm{adv}} + F^s_{\mathrm{diff}}$ and the diahaline salinity fluxes defined in (4).

According to Burchard (2020), the mixing per salinity class $m(S)$ is defined as

$$m(S) = \partial_S M(S) \text{ with } M(S) = \int_0^S m\left(S'\right)\mathrm{d}S' = \left\langle \int_{V(S)} \chi \,\mathrm{d}V \right\rangle, \tag{13}$$

with the integrated salinity mixing $M(S)$. Note that (13) has already been formulated by Wang et al. (2017) for the vertical component of mixing, see their eq. (4.3). Combining (5) and (9), the mixing per salinity class can also be formulated as

$$\begin{aligned} m &= \left\langle \int_{A(S)} (\partial_n s)^{-1} \chi \,\mathrm{d}A \right\rangle \\ &= \left\langle \int_{A(S)} (\partial_n s)^{-1} 2K_n (\partial_n s)^2 \,\mathrm{d}A \right\rangle \\ &= 2\left\langle \int_{A(S)} K_n \partial_n s \,\mathrm{d}A \right\rangle \\ &= -2F^s_{\mathrm{diff}}. \end{aligned} \tag{14}$$

With this, the mixing per salinity class is twice the (negative) diahaline turbulent salinity transport. This also means that the mixing integrated over the volume $V(S)$ can be expressed by means of integrating the turbulent diahaline salinity transport through all isohalines with salinities smaller than or equal to S:

$$-2\int_0^S F^s_{\mathrm{diff}} \,\mathrm{d}S' = M(S), \tag{15}$$

see eq. (4.4) by Wang et al. (2017). Eq. (14) allows for easy calculation of diahaline turbulent transport and effective diahaline diffusivities including their decomposition into physically and numerically induced components (see below). This formulation does also allow formulating the recently proposed universal law of estuarine mixing (Burchard 2020) without using a budget equation for the salinity variance or the integrated salinity square, see Sec. 2d.

Following Klingbeil et al. (2014), the mixing per unit volume χ can be exactly decomposed into physical and numerical contributions, such that consequently also the mixing per isohaline volume can be decomposed:

$$m = m^{\mathrm{phy}} + m^{\mathrm{num}}. \tag{16}$$

Motivated by the relations in (5), the effective total diahaline diffusivity, $\overline{K_n}$, can be calculated by dividing the negative mean diahaline turbulent flux averaged over the isohaline surface, $-F^s_{\mathrm{diff}}/a = \frac{1}{2}m/a$, by the mean diahaline salinity gradient, $b^{-1} = a/v$:

$$\overline{K_n} = \frac{-F^s_{\mathrm{diff}}/a}{b^{-1}} = \frac{1}{2}\frac{mv}{a^2}. \tag{17}$$

Using (16), the effective diahaline diffusivity can be split into physical and numerical parts:

$$\overline{K_n^{\mathrm{phy}}} = \frac{1}{2}\frac{m^{\mathrm{phy}}v}{a^2}, \quad \overline{K_n^{\mathrm{num}}} = \frac{1}{2}\frac{m^{\mathrm{num}}v}{a^2}. \tag{18}$$

Details of the discretization of (18) are given in section 3.

d. Diahaline mixing relations

As shown in Burchard (2020) for tidally periodic estuaries averaged over a tidal period or general estuaries averaged over a long period, the down-estuarine advective salt transport through an isohaline of salinity S is $F^s_{\mathrm{adv}} = SQ_r$, where Q_r is the river run-off. Under these equilibrium conditions, the down-estuarine advective salt transport must be exactly balanced by an opposing up-estuarine diffusive salt transport $F^s_{\mathrm{diff}} = -F^s_{\mathrm{adv}}$. Using (14), we obtain $m = -2F^s_{\mathrm{diff}} = 2F^s_{\mathrm{adv}} = 2SQ_r$, stating that under equilibrium conditions the mixing per salinity class is twice the product of the river run-off times the salinity of the respective isohaline. This has been recently formulated by Burchard

(2020) as the universal law of estuarine mixing, derived by combining volume-integrated budget equations for volume, salinity and salinity squared.

3. Discretization

The numerical model calculates for each time step n and for each grid box i,k discrete values for the layer thickness, $h_{i,k}^n$, the salinity, $s_{i,k}^n$, the physical mixing per unit volume, $\chi_{i,k}^{\mathrm{phy},n}$ (due to diffusion with eddy diffusivity calculated by the turbulence closure scheme), and the numerical mixing per unit volume, $\chi_{i,k}^{\mathrm{num},n}$ (due to truncation errors of the salinity advection scheme). The latter two quantities are calculated by means of the method proposed by Klingbeil et al. (2014) as local discrete variance decay due to diffusion and advection, respectively. Furthermore, the horizontal grid cell area is kept constant in time and is denoted as A_i. The index i is here the counter for the two-dimensional horizontal grid which may be structured or unstructured, and k is the vertical counter of layers.

For the binning into salinity classes, the salinity range $s_{\min} \le s \le s_{\max}$ is discretized into J equidistant salinity intervals $\Delta s = (s_{\max} - s_{\min})/J$. The time-averaged volume per salinity class, v_j, is then calculated for each water column i as

$$v_{i,j} = \frac{A_i}{N\Delta s} \sum_{\substack{k,n \\ \{s_{j-1} \le s_{i,k}^n < s_j\}}} h_{i,k}^n, \quad \text{with} \quad j = \left\lceil \frac{s_{i,k}^n - s_{\min}}{s_{\max} - s_{\min}} J \right\rceil, \tag{19}$$

where $s_j = s_{\min} + j\Delta s$ and $\lceil x \rceil$ is the ceiling function to any non-negative real number x, j with $1 \le j \le J$ is the counter for the salinity class and N is the number of time steps. With (19), a vector of salinity classes j is defined for each water column i which is then subsequently filled in a binning process with subvolumes $A_i h_{i,k}^n$ and averaged by the number of time steps N. Division by Δs is necessary in (19), because $v_{i,j}$ is volume per salinity class.

The physical and numerical mixing per salinity class, $m_{i,j}^{\text{phy}}$ and $m_{i,j}^{\text{num}}$, are calculated accordingly as

$$m_{i,j}^{\text{phy}} = \frac{A_i}{N\Delta s} \sum_{\substack{k,n \\ \{s_{j-1} \le s_{i,k}^n < s_j\}}} \chi_{i,k}^{\text{phy},n} h_{i,k}^n, \quad m_{i,j}^{\text{num}} = \frac{A_i}{N\Delta s} \sum_{\substack{k,n \\ \{s_{j-1} \le s_{i,k}^n < s_j\}}} \chi_{i,k}^{\text{num},n} h_{i,k}^n. \tag{20}$$

Let $A = \sum_{i \in I} A_i$ be a specifically defined sub-area (e.g., an estuarine segment or the entire estuary) composed of all areas A_i with the index i included in the set I. Then, following (18), with (19) and (20), the physical and numerical effective diahaline diffusivities for $A(S = s_j)$ are calculated as

$$\overline{K_j^{\text{phy}}} = \frac{\sum_{i \in I} m_{i,j}^{\text{phy}} \cdot \sum_{i \in I} v_{i,j}}{2\left(\sum_{i \in I} a_{i,j}\right)^2}, \quad \overline{K_j^{\text{num}}} = \frac{\sum_{i \in I} m_{i,j}^{\text{num}} \cdot \sum_{i \in I} v_{i,j}}{2\left(\sum_{i \in I} a_{i,j}\right)^2}, \tag{21}$$

with the isohaline area

$$a_{i,j} = \begin{cases} A_i, & \text{if } v_{i,j} > 0 \\ 0, & \text{else.} \end{cases} \tag{22}$$

With (22), a water column with an empty salinity class j is associated with zero isohaline area. This may happen, when a salinity class is outside the range of salinities occurring in a water column (such as ocean salinity in permanently brackish water). This may also happen for high numbers of salinity classes and low numbers of salinity values (due to low vertical and temporal resolution or short averaging periods). In both cases, such empty salinity classes pose no problem. If a salinity class does not occur in any water column of the chosen sub-area, the effective diahaline diffusivities for that salinity class are not defined. It should be mentioned here, that $A(S = s_j)$ is the projection of the isohaline surface to geopotential surfaces, an error that is small due to the small aspect ratio of estuaries (see also the results of Sec. 4) and it is identical for the calculation of both, the effective physical and numerical diahaline diffusivity.

4. Idealized model experiments

To demonstrate the calculation of effective diahaline diffusivities and other mixing-related properties, we simulate an idealized estuary, exponentially widening towards the open ocean (Fig. 4). The estuary is situated at a latitude of 53.5°N and has a length of 100 km, a central navigational channel of 15 m depth, and lateral shoals with an average depth of 3 m. At the mouth, the estuary is 81 km wide to allow for the development of a river plume, and decreases in width exponentially in landward direction. The minimum width of the estuarine channel is set to 1 km. The model is forced at the open boundary with a mono-chromatic semi-diurnal tide of 2.0 m amplitude and a constant ocean salinity of 35 g/kg. At the river end of the estuary, a constant freshwater run-off of $Q_r = 700\ \mathrm{m^3 s^{-1}}$ is prescribed. There is no wind forcing applied.

For the simulations, the General Estuarine Transport Model (GETM, `www.getm.eu`, Burchard and Bolding 2002) has been applied, a primitive equation coastal ocean model model using general vertical coordinates and explicit mode splitting (Klingbeil et al. 2018). It is coupled to the turbulence module of the General Ocean Turbulence Model (GOTM, `www.gotm.net`, Burchard and Bolding 2001; Umlauf and Burchard 2005), using the k-ε two-equation turbulence closure model with an algebraic second-moment closure by Cheng et al. (2002). Explicit horizontal diffusion is not applied.

A curvi-linear grid is constructed with 200 cells in longitudinal direction and 30 cells across the estuary. In the vertical, 30 σ-layers are used with some grid refinement towards the bottom. For the temporal discretization, each tidal cycle is resolved with 5000 baroclinic time steps of $\Delta t = 8,9428$ s, each of them split into 10 barotropic time steps. The advection terms in the momentum, salinity and turbulence budgets are discretized by means of the TVD-SPL-max-1/3 scheme

(Waterson and Deconinck 2007), known for its minimum numerical mixing (Mohammadi-Aragh et al. 2015), combined with Strang splitting (Pietrzak 1998).

The simulation is started from rest (zero surface elevation, zero velocity, constant salinity $s = 15$ g/kg) until a quasi-periodic state is reached, still including non-tidal oscillations such as internal waves of frequencies not matching the tidal frequency. Ten tidal periods of this quasi-periodic state are analyzed to calculate representative tidally averaged properties.

A snapshot of the salinity distribution at high water is shown in Fig. 4. A salt wedge is reaching up to kilometer 70 of the estuary with a strong near-surface stratification downstream of it. A river plume veering to the north (positive y-direction) due to Earth rotation is visible in the outer estuary. The lateral salinity structure is complex due to lateral circulation (which is not shown).

The salinity fields from the TEF-based averaging and the thickness-weighted averaging are shown in Fig. 5 for the center line of the estuary ($y = 0$). It should be noted that both fields do not show the average salinity at the specific coordinate in x-z space where they have occurred. For each water column, the TEF-based average salinity is located at $z^{\mathrm{TEF}}(S)$ defined in (11). With this, the lowest salinity occurring in that water column is located at the time-averaged surface, and the highest salinity is located at the bottom. As for the thickness-weighted averaging, the salinity field has first been averaged on σ-layers with weighting by the changing water depth, and then the averaged salinity values have been associated with the average vertical position of the respective σ layer (see the discussion by Klingbeil et al. 2019). Clearly, the TEF-based isohalines are more widespread, i.e., have a larger surface, than the isohalines from thickness-averaging. For instance, the TEF-based isohaline with $S = 25$ g/kg at $y = 0$ (marked in red) is twice as long as the thickness-averaged isohaline (30 km versus 15 km). This is because whenever a specific salinity has occurred within a water column, the respective isohaline extends to this horizontal position. In contrast, thickness-weighted averaging might not show this salinity in a water column.

Despite the substantially different appearances of the two salinity fields, the associated isohaline volumes are the same, see the discussion in Sec. 2b. Here, it can also be seen how small the error of approximating the isohaline area by its projection to geopotential coordinates is: for the example of the 25-g/kg-isohaline based on TEF (Fig. 5a), the relative error of the isohaline area is $1-L/(H^2+L^2)^{1/2}=2.5\cdot 10^{-7}$, with the length of the projected isohaline of $L=30$ km and the centerline depth of $H=15$ m, when assuming a flat bottom and a planar approximation of the isohaline.

Since physical lateral diffusivity is set to zero in the model experiment, it is expected according to (5) and (17) that the effective physical diahaline diffusivities, $\overline{K_n^{\mathrm{phy}}}$, are a weighted average of the vertical diffusivities, K_v, occurring in a specific salinity class. This should also be the case for the effective total diahaline diffusivities, $\overline{K_n}$, when physical mixing is dominating over numerical mixing. It is therefore instructive to inspect the distributions of K_v for different situations. This is shown in Fig. 6 as snapshots during full flood and full ebb for the centerline of the estuary. During flood, due to a destabilization of the lower half of the water column in the salt wedge vertical diffusivity is enhanced in this region with values of around $K_v=10^{-2}$ m^{2}s^{-1}. During ebb, marginal shear instability is dominating in parts of the salt wedge (with salinities above 12 g/kg) such that vertical diffusivities are still elevated, but when strong stratification occurs too close to the bed, the eddy diffusivity in the water column above drops to values of below 10^{-5} m^{2}s^{-1}. When isohalines are flat, diffusivities are mostly below 10^{-5} m^{2}s^{-1}. Since flat regions of the isohalines are associated with the largest portion of area, it is expected that effective physical diahaline diffusivities are of the order of 10^{-5} m^{2}s^{-1}. In the well-mixed regions upstream (near $s=0$ g/kg) and downstream (near $s=35$ g/kg) of the salt wedge, diffusivities reach high values of up to 10^{-1} m^{2}s^{-1}.

The analysis of mixing per salinity class shows that the universal law of estuarine mixing proposed by Burchard (2020) is closely approximated by averaging over 10 tidal periods in a quasi-periodic state (Fig. 7a). For salinities below 22 g/kg (the maximum salinity that is not reaching the open boundary) physical mixing is dominating the total mixing with numerical mixing only contributing by about 30 % at most. Only in the coarse resolution region of the river plume at salinities larger than 30 g/kg numerical mixing is dominating (Fig. 7a). As further input to the calculation of effective diahaline diffusivity, volume per salinity class and isohaline area (Fig. 7b), and the mean salinity gradient of each salinity class, b^{-1} (Fig. 7c) are shown. Maximum values of b^{-1} of more than 10 (g/kg) m^{-1} are reached between salinities 16 g/kg and 23 g/kg. This means that for those salinity classes the isohalines are so much stretched out in longitudinal direction that the thickness per salinity class decreases below 0.1 m (g/kg)$^{-1}$, see also Fig. 5b. With m, v and a (Figs. 7a and 7b), all parameters determining the effective diahaline diffusivities are present. The resulting diffusivities are shown in Fig. 7d. $\overline{K_n}$ increases about linearly from $1 \cdot 10^{-5}$ m^{2}s^{-1} at a salinity of 1 g/kg to a maximum of $6 \cdot 10^{-5}$ m^{2}s^{-1} at 7 g/kg and then decreases to $1 \cdot 10^{-5}$ m^{2}s^{-1} at 23 g/kg. A peak in effective diahaline diffusivity is generated by a combination of the mixing per salinity class and the isohaline area increasing with salinity and the volume per salinity class substantially dropping down above a salinity of 7 g/kg. For salinities larger than 23 g/kg, the effective diahaline diffusivity reaches a relative high level of $\geq 2 \cdot 10^{-5}$ m^{2}s^{-1}, with a peak of $1 \cdot 10^{-4}$ m^{2}s^{-1} at 24 g/kg, due to a high isohaline volume per salinity class and a consequently small diahaline gradient. As for the mixing per salinity class, also for the effective diahaline diffusivity, the numerical contribution is high. Generally, effective diahaline diffusivities are substantially lower than the relative high instantaneous values of $K_v > 10^{-2}$ m^{2}s^{-1} shown in Fig. 6 for the well-mixed regions in the freshwater range, the bottom boundary layer and the well-mixed region near the mouth. This can be explained by the fact that the mixing per unit volume, χ, is generally low in these regions, which has an impact on the mixing per salinity class, m.

To analyze the spatial distribution of total mixing per salinity class, an integration along the transverse coordinate is carried out, such that total mixing per salinity class per longitudinal distance is calculated, see Fig. 8. As a result, elevated mixing occurs over a large range of distance and salinity classes. Integration of the total mixing per salinity class and meter with respect to x results in total mixing per salinity class approximating the universal law (left graph). When integrating with respect to salinity, total mixing per meter is obtained, see the upper graph in Fig. 8, showing maximum values in the range -90 km $\leq x \leq -80$ km. However, this distribution does not follow a specific law. Together with the volume per salinity class per longitudinal distance (Fig. 9a), the effective total diahaline diffusivity can be calculated (Fig. 9b). There is a broad region in salinity and longitudinal distance where the effective total diahaline diffusivity is of the order of 10^{-4} m^{2}s^{-1}. At some distinct locations (-80 km $\leq x \leq -70$ km, $S \leq 15$ g/kg), elevated values of up to $5 \cdot 10^{-4}$ m^{2}s^{-1} occur due to a combination of localized high mixing and high volume.

Using the information on mixing per salinity class and volume per salinity class for every water column, it is possible to calculate maps of the effective diahaline diffusivity, as shown in Fig. 10a-c for the example of $S = 25$ g/kg. In the well-resolved channelized region of the estuary ($x \geq -90$ km), diffusivities are dominated by physical values. They are highest in the deeper parts of the channel and reach values of several 10^{-4} m^{2}s^{-1}. Over the shoals, the diffusivities are about one order of magnitude smaller. In the region of the outer estuary ($x \leq -90$ km), where the river plume veers to the right in downstream direction due to Earth rotation, the horizontal resolution becomes coarse, such that numerical mixing is comparable to physical mixing (Fig. 10b,c). With this, the maps of Fig. 10a-c represent the spatial distribution of the effective diahaline total, physical and numerical diffusivities that are accumulated to one value for each salinity in Fig. 7d. As an example, the effective physical diahaline diffusivity is $\overline{K_n^{\mathrm{phy}}}(S = 25\,\mathrm{g/kg}) = 2 \cdot 10^{-5}\ \mathrm{m^2s^{-1}}$ (Fig. 7d), which can be interpreted as a weighted integral average of the spatial distribution of $\overline{K_n^{\mathrm{phy}}}(S = 25\,\mathrm{g/kg}, x, y)$ over all water columns x and y where the salinity of 25 g/kg is occurring at least once during the averaging interval.

5. Discussion

The major goal of this study is to develop a method to calculate effective diahaline turbulent fluxes and diffusivities, including a decomposition into physical and numerical contributions. The resulting method is based on the calculation of mixing per salinity class from which diahaline transports can directly be derived, see (14), as well as on the calculation of volume per salinity class, a concept which had already been proposed by Walin (1977). The method is robust in the sense that no interpolations to isohaline surfaces in numerical models are needed and that the resulting effective turbulent diahaline transport is always negative (i.e., down-gradient) and effective diahaline diffusivities are positive definite, except for unlikely situations when negative mixing by anti-diffusive advection schemes dominates the effective total diahaline diffusivity. The only inaccuracy in the calculation of the effective diahaline diffusivities is the determination of the isohaline surface for which we use the projection to geopotential surfaces. However, as visible in Fig. 5a, even in estuaries isohaline surfaces based on TEF analysis are relatively flat, such the error associated with their slope should be negligible.

The main product of the present study are maps of the effective diahaline diffusivities, as shown in Fig. 10 for the isohaline of $S = 25$ g/kg. Such maps could be shown for all salinity classes and give a clear picture about the mixing hotspots and physical and numerical contributions. Effective diahaline diffusivities as statistical diagnostics for estuarine models are distinct from instantaneous diffusivities which in well-mixed regions can be orders of magnitude larger. The calculation of effective diahaline diffusivities can be viewed as a complex weighted spatial and temporal averaging process, where high instantaneous diffusivities in well-mixed regions have small weights due to their small contribution to mixing.

Although diffusivities are defined as the (negative) ratio between a turbulent flux and the associated gradient of the transported property and as such their (un-weighted) average in time and space is not a useful property, they are key quantities for diagnosing mixing processes in the ocean. Using the Osborn and Cox (1972) and Osborn (1980) methods based on equilibrium versions of the tracer variance and turbulent kinetic energy budgets respectively, diapycnal eddy diffusivities can be calculated which in turn can be used to calculate diapycnal tracer fluxes.

In ocean models, complex and computationally demanding turbulence closure schemes are used to compute eddy diffusivities (see, e.g., Large et al. 1994; Umlauf and Burchard 2005). Except for situations of double diffusion (Canuto et al. 2002) eddy diffusivities are assumed to be same for all tracers, a concept that underlines their relevance. However, in ocean models, when explicit horizontal diffusivity is not aligned with the diahaline surface, instantaneous diahaline diffusivities are different for each tracer, as seen from (5). Also, numerical mixing (and therefore numerical diffusivity) depends strongly on the tracer gradients and is thus different for all tracers (Burchard and Rennau 2008). Moreover, effective diahaline diffusivities as calculated from (17) depend on the tracer under consideration. On the other hand, a field and modeling study in the deep water of the Central Baltic Sea showed that the diagnosed profile of effective diapycnal diffusivity could explain the evolution of salinity, temperature and an injected tracer over several years (Holtermann et al. 2012, 2014). The method developed here can only calculate the effective tracer diffusivities orthogonal to isosurfaces of the respective tracer. Still, as shown in Fig. 10, it is a useful diagnostics for estuarine mixing processes and their representation in numerical models.

Whereas the salinity mixing per salinity class as well as the diahaline salt transport averaged over a long time converge towards theoretical limits (Burchard 2020), no such theories exist for isohaline volumes or effective diahaline diffusivities. Those depend on the individual dynamics of the estuary which in turn is mainly triggered by the bathymetry and the freshwater and tidal forcing.

In estuaries salinity dominates density stratification such that the calculation of diahaline mixing and diffusivities are a relevant diagnostics for the dynamics. However, outside estuaries, density stratification is generally depending on both, salinity and temperature. Since in most ocean models density is directly transported neither by advection nor by diffusion, physical and numerical mixing of density cannot be calculated directly. Instead, in order to diagnose diapycnal turbulent density fluxes and effective density diffusivities in ocean models, physical and numerical mixing of temperature and salinity need to be combined in a suitable way. Such a diagnostics would allow adding spatial resolution to the bulk estimates of diapycnal diffusivities proposed by various authors (Griffies et al. 2000; Lee et al. 2002; Getzlaff et al. 2010, 2012; Ilıcak et al. 2012; Megann 2018).

6. Conclusions

A method has been developed to diagnose effective diahaline diffusivities in numerical models of estuaries. It is based on the calculation of volume per salinity class and mixing per salinity class, the former having been proposed already by Walin (1977) whereas the latter has only recently been developed by Wang et al. (2017) and Burchard (2020). In numerical models, effective diahaline diffusivities consist of physical (from turbulence parameterizations) and numerical (from discretization errors of advection schemes) contributions and add exactly up to the effective total diahaline diffusivity. The calculation therefore requires the analysis of physical and numerical mixing as introduced by Burchard and Rennau (2008) and Klingbeil et al. (2014).

The method computes generally positive values for effective physical and numerical diahaline diffusivities for each salinity class and each water column (unless anti-diffusive advection schemes are used), whenever the respective salinity has occurred in the water column during the averaging period. Based on this water column information, effective diahaline diffusivities can be aggregated in various dimensions, either as horizontal maps of diffusivity for a specified salinity class, as function of salinity and longitudinal distance, or as function of salinity only, always showing physical and numerical values as well as the sum of both.

These diagnostics help to understand where mixing is strong in an estuary and indicate where numerical mixing is high. The latter helps to plan measures for reducing numerical artifacts by choosing a higher model resolution, better advection schemes or, as the ultimate measure, to reduce physical mixing in order to limit effective total diahaline mixing to realistic levels (Ralston et al. 2017). In the idealized simulations carried out in the present study, numerical diffusivities were on acceptable levels in the inner estuary, but due the coarse resolution of the outer estuary, they dominated the dynamics in the region.

Acknowledgments. This paper is a contribution to the Collaborative Research Centre TRR 181 on Energy Transfers in Atmosphere and Ocean and the Research Training Group Baltic TRANSCOAST GRK 2000 funded by the German Research Foundation.

References

Beckers, J. M., Burchard, H., Campin, J. M., Deleersnijder, E., Matthieu, P. P., 1998. Another reason why simple discretizations of rotated diffusion operators cause problems in ocean models: Comments on *isoneutral diffusion in a z-coordinate ocean model*. J. Phys. Oceanogr. 28, 1552–1559.

Blumberg, A. F., Mellor, G. L., 1987. A description of a three-dimensional coastal ocean circulation model. Three-dimensional coastal ocean models, 1–16.

Burchard, H., 2020. A universal law of estuarine mixing. J. Phys. Oceanogr. 50, 81–93.

Burchard, H., Bolding, K., 2001. Comparative analysis of four second-moment turbulence closure models for the oceanic mixed layer. J. Phys. Oceanogr. 31, 1943–1968.

Burchard, H., Bolding, K., 2002. GETM – a general estuarine transport model. Scientific documentation. Tech. Rep. EUR 20253 EN, European Commission.

Burchard, H., Janssen, F., Bolding, K., Umlauf, L., Rennau, H., 2009. Model simulations of dense bottom currents in the Western Baltic Sea. Cont. Shelf Res. 29, 205–220.

Burchard, H., Lange, X., Klingbeil, K., MacCready, P., 2019. Mixing estimates for estuaries. J. Phys. Oceanogr. 49, 631–648.

Burchard, H., Rennau, H., 2008. Comparative quantification of physically and numerically induced mixing in ocean models. Ocean Model. 20, 293–311.

Canuto, V. M., Howard, A., Cheng, Y., Dubovikov, M. S., 2002. Ocean turbulence. Part II: Vertical diffusivities of momentum, heat, salt, mass, and passive scalars. J. Phys. Oceanogr. 32, 240–264.

Cheng, Y., Canuto, V., Howard, A., 2002. An improved model for the turbulent PBL. J. Atmos. Sci. 59, 1550–1565.

Fischer, H. B., 1976. Mixing and dispersion in estuaries. Annu. Rev. Fluid Mech. 8, 107–133.

Getzlaff, J., Nurser, G., Oschlies, A., 2010. Diagnostics of diapycnal diffusivity in z-level ocean models. Part I: 1-dimensional case studies. Ocean Model. 35, 173–186.

Getzlaff, J., Nurser, G., Oschlies, A., 2012. Diagnostics of diapycnal diffusion in z-level ocean models. Part II: 3-dimensional OGCM. Ocean Model. 45, 27–36.

Geyer, W. R., Trowbridge, J. H., Bowen, M. M., 2000. The dynamics of a partially mixed estuary. J. Phys. Oceanogr. 30, 2035–2048.

Goudsmit, G.-H., Peeters, F., Gloor, M., Wüest, A., 1997. Boundary versus internal diapycnal mixing in stratified natural waters. J. Geophys. Res. 102, 2790327914.

Griffies, S. M., Gananadesikan, A., Pacanowski, R., Larichev, V., Dukowicz, J., Smith, R., 1998. Isoneutral diffusion in a z-coordinate ocean model. J. Phys. Oceanogr. 28, 805–830.

Griffies, S. M., Pacanowski, R. C., Hallberg, R. W., 2000. Spurious diapycnal mixing associated with advection in a z-coordinate ocean model. Monthly Weather Rev. 128, 538–564.

Hansen, D. V., Rattray, M., 1965. Gravitational circulation in straits and estuaries. J. Mar. Res. 23, 104–122.

Hetland, R. D., 2005. Relating river plume structure to vertical mixing. J. Phys. Oceanogr. 35, 1667–1688.

Hetland, R. D., Geyer, W. R., 2004. An idealized study of the structure of long, partially mixed estuaries. J. Phys. Oceanogr. 34, 2677–2691.

Hofmeister, R., Beckers, J.-M., Burchard, H., 2011. Realistic modelling of the exceptional inflows into the central Baltic Sea in 2003 using terrain-following coordinates. Ocean Model. 39, 233–247.

Holtermann, P. L., Burchard, H., Gräwe, U., Klingbeil, K., Umlauf, L., 2014. Deep-water dynamics and boundary mixing in a nontidal stratified basin: A modeling study of the Baltic Sea. J. Geophys. Res. 119, doi:10.1002/2013JC009483.

Holtermann, P. L., Umlauf, L., Tanhua, T., Schmale, O., Rehder, G., Waniek, J., 2012. The Baltic Sea Tracer Release Experiment: 1. Mixing rates. J. Geophys. Res. 117, doi:10.1029/2011JC007439.

Ilıcak, M., Adcroft, A. J., Griffies, S. M., Hallberg, R. W., 2012. Spurious dianeutral mixing and the role of momentum closure. Ocean Model. 45, 37–58.

Klingbeil, K., Becherer, J., Schulz, E., de Swart, H. E., Schuttelaars, H. M., Valle-Levinson, A., Burchard, H., 2019. Thickness-Weighted Averaging in tidal estuaries and the vertical distribution of the Eulerian residual transport. J. Phys. Oceanogr. 49, 1809–1826.

Klingbeil, K., Lemarié, F., Debreu, L., Burchard, H., 2018. The numerics of hydrostatic structured-grid coastal ocean models: State of the art and future perspectives. Ocean Modell. 125, 80–105.

Klingbeil, K., Mohammadi-Aragh, M., Gräwe, U., Burchard, H., 2014. Quantification of spurious dissipation and mixing - Discrete variance decay in a finite-volume framework. Ocean Model. 81, 49–64.

Large, W. G., McWilliams, J. C., Doney, S. C., 1994. Oceanic vertical mixing: a review and a model with nonlocal boundary layer parameterisation. Rev. Geophys. 32, 363–403.

Largier, J. L., Hearn, C. J., Chadwick, D. B., 1996. Density structures in low inflow estuaries. In: Aubrey, D. G., Friedrichs, C. T. (Eds.), Buoyancy Effects on Coastal and Estuarine Dynamics. Vol. 53 of Coastal and Estuarine Studies. American Geophysical Union, pp. 227–241.

Lee, M.-M., Coward, A. C., Nurser, A. J. G., 2002. Spurious diapycnal mixing of the deep waters in an eddy-permitting global ocean model. J. Phys. Oceanogr. 32, 1522–1535.

Li, X., Geyer, W. R., Zhu, J., Wu, H., 2018. The transformation of salinity variance: A new approach to quantifying the influence of straining and mixing on estuarine stratification. J. Phys. Oceanogr. 48, 607–623.

Linden, P. F., Simpson, J. E., 1986. Gravity-driven flows in a turbulent fluid. J. Fluid Mech. 172, 481–497.

Linden, P. F., Simpson, J. E., 1988. Modulated mixing and frontogenesis in shallow seas and estuaries. Cont. Shelf Res. 8, 1107–1127.

MacCready, P., 2011. Calculating estuarine exchange flow using isohaline coordinates. J. Phys. Oceanogr. 41 (6), 1116–1124.

MacCready, P., Geyer, W. R., 2001. Estuarine salt flux through an isohaline surface. J. Geophys. Res. 106, 11629–11637.

MacCready, P., Geyer, W. R., Burchard, H., 2018. Estuarine exchange flow is related to mixing through the salinity variance budget. J. Phys. Oceanogr. 48, 1375–1384.

MacCready, P., Hetland, R. D., Geyer, W. R., 2002. Long-term isohaline salt balance in an estuary. Cont. Shelf Res. 22, 1591–1601.

Megann, A., 2018. Estimating the numerical diapycnal mixing in an eddy-permitting ocean model. Ocean Model. 121, 19–33.

Mohammadi-Aragh, M., Klingbeil, K., Brüggemann, N., Eden, C., Burchard, H., 2015. The impact of advection schemes on restratifiction due to lateral shear and baroclinic instabilities. Ocean Modell. 94, 112–127.

Osborn, T. R., 1980. Estimates of the local rate of vertical diffusion from dissipation measurements. J. Phys. Oceanogr. 10, 83–89.

Osborn, T. R., Cox, C. S., 1972. Oceanic fine structure. Geophys. Astrophys. Fluid Dyn. 3, 321–345.

Pietrzak, J., 1998. The use of TVD limiters for forward-in-time upstream-biased advection schemes in ocean modeling. Mon. Weather Rev. 126, 812–830.

Ralston, D. K., Cowles, G. W., Geyer, W. R., Holleman, R. C., 2017. Turbulent and numerical mixing in a salt wedge estuary: Dependence on grid resolution, bottom roughness, and turbulence closure. J. Geophys. Res. 122, 692–712.

Ralston, D. K., Geyer, W. R., Lerczak, J. A., 2008. Subtidal salinity and velocity in the Hudson River estuary: Observations and modeling. J. Phys. Oceanogr. 38, 753–770.

Taylor, G. I., 1954. The dispersion of matter in turbulent flow through a pipe. Proc. R. Soc. London. Ser. A 223, 446–468.

Umlauf, L., Burchard, H., 2005. Second-order turbulence models for geophysical boundary layers. A review of recent work. Cont. Shelf Res. 25, 795–827.

Uncles, R. J., Stephens, J. A., 1990. Computed and observed currents, elevations, and salinity in a branching estuary. Estuaries 13, 133–144.

Walin, G., 1977. A theoretical framework for the description of estuaries. Tellus 29, 128–136.

Wang, T., Geyer, W. R., MacCready, P., 2017. Total exchange flow, entrainment, and diffusive salt flux in estuaries. J. Phys. Oceanogr. 47, 1205–1220.

Warner, J. C., Geyer, W. R., Lerczak, J. A., 2005. Numerical modeling of an estuary: A comprehensive skill assessment. J. Geophys. Res. 110, 10.1029/2004JC002691.

Waterhouse, A. F., MacKinnon, J. A., Nash, J. D., Alford, M. H., Kunze, E., Simmons, H. L., Polzin, K. L., St. Laurent, L. C., Sun, O. M., Pinkel, R., Talley, L. D., Whalen, C. B., Huussen, T. N., Carter, G. S., Fer, I., Waterman, S., Naveira Garabato, A. C., Sanford, T. S., Lee, C. M., 2014. Global patterns of diapycnal mixing from measurements of the turbulent dissipation rate. J. Phys. Oceanogr. 44, 1854–1872.

Waterson, N. P., Deconinck, H., 2007. Design principles for bounded higher-order convection schemes - a unified approach. J. Comput. Phys. 224, 182–207.

Young, W., Jones, S., 1991. Shear dispersion. Physics of Fluids A: Fluid Dynamics 3, 1087–1101.

LIST OF TABLES

Symbol	meaning	unit
a^{TEF}, a^{Eu}	TEF-based and Eulerian isohaline area	m^2
A	instantaneous isohaline surface	m^2
A_r	river transect area	m^2
b^{TEF}, b^{Eu}	TEF-based and Eulerian isohaline thickness	$\mathrm{m}\,(\mathrm{g/kg})^{-1}$
b^{loc}	local thickness per salinity class	$\mathrm{m}\,(\mathrm{g/kg})^{-1}$
B^{loc}	accumulated local thickness	m
f^s	diahaline salinity flux	$\mathrm{m\,s}^{-1}(\mathrm{g/kg})$
f^s_{adv}	advective diahaline salinity flux	$\mathrm{m\,s}^{-1}(\mathrm{g/kg})$
f^s_{diff}	diffusive diahaline salinity flux	$\mathrm{m\,s}^{-1}(\mathrm{g/kg})$
F^s	diahaline salinity transport	$\mathrm{m}^3\mathrm{s}^{-1}(\mathrm{g/kg})$
F^s_{adv}	advective diahaline salinity transport	$\mathrm{m}^3\mathrm{s}^{-1}(\mathrm{g/kg})$
F^s_{diff}	diffusive diahaline salinity transport	$\mathrm{m}^3\mathrm{s}^{-1}(\mathrm{g/kg})$
$\vec{\mathscr{F}}^s_{\mathrm{diff}}$	diffusive salinity flux vector	$\mathrm{m\,s}^{-1}(\mathrm{g/kg})$
K_h	horizontal eddy diffusivity	$\mathrm{m}^2\mathrm{s}^{-1}$
K_n	diahaline eddy diffusivity	$\mathrm{m}^2\mathrm{s}^{-1}$
$\overline{K_n}$	effective total diahaline diffusivity	$\mathrm{m}^2\mathrm{s}^{-1}$
$\overline{K_n^{\mathrm{num}}}$	effective numerical diahaline diffusivity	$\mathrm{m}^2\mathrm{s}^{-1}$
$\overline{K_n^{\mathrm{phy}}}$	effective physical diahaline diffusivity	$\mathrm{m}^2\mathrm{s}^{-1}$
K_v	vertical eddy diffusivity	$\mathrm{m}^2\mathrm{s}^{-1}$
m	mixing per salinity class	$\mathrm{m}^3\mathrm{s}^{-1}$ (g/kg)
m^{num}	numerical mixing per salinity class	$\mathrm{m}^3\mathrm{s}^{-1}$ (g/kg)
m^{phy}	physical mixing per salinity class	$\mathrm{m}^3\mathrm{s}^{-1}$ (g/kg)
M	volume-integrated mixing	$\mathrm{m}^3\mathrm{s}^{-1}\ (\mathrm{g/kg})^2$
$\vec{u}$	velocity vector	$\mathrm{m\,s}^{-1}$
u_n	diahaline velocity	$\mathrm{m\,s}^{-1}$
s	absolute salinity	$\mathrm{g\,kg}^{-1}$
v	volume per salinity class	$\mathrm{m}^3(\mathrm{g/kg})^{-1}$
V	accumulated estuarine volume	m^3
χ	salinity mixing per unit volume	$\mathrm{s}^{-1}(\mathrm{g/kg})^2$
z^{TEF}, z^{Eu}	TEF-based and Eulerian isohaline position	m

TABLE 1. List of variables including their meanings and units.

LIST OF FIGURES

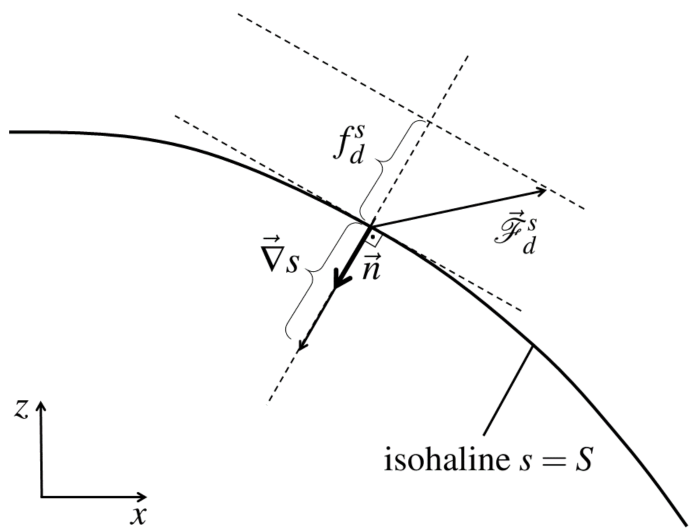

FIG. 1. Sketch explaining the projection of the turbulent diffusive flux vector $\vec{\mathscr{F}}^s_{\mathrm{diff}}$ to the diahaline direction. The unit normal vector $\vec{n}$ is pointing outside the domain towards higher salinity.

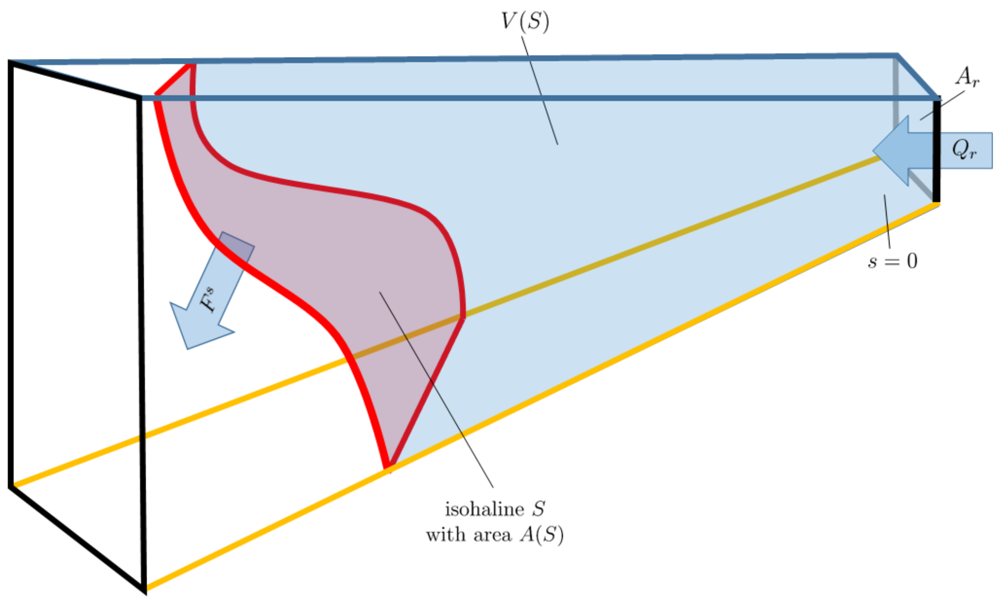

FIG. 2. Sketch explaining the volume-integrated budgets with respect to the transect and the isohaline S.

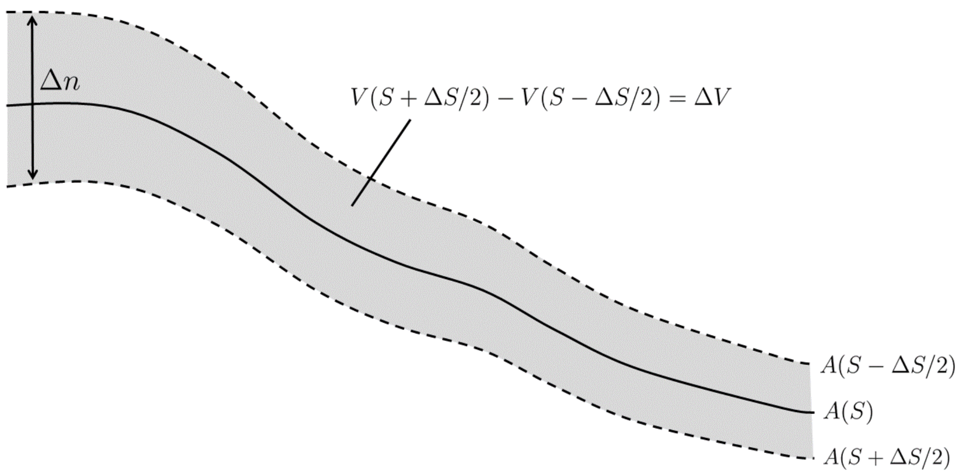

FIG. 3. Sketch explaining the isohaline volume and thickness by means of a finite salinity increment ΔS. The gray area indicates the finite volume ΔV between the isohaline surfaces $A(S+\Delta S/2)$ and $A(S-\Delta S/2)$. For the limit of $\Delta S \to 0$, $\Delta V/\Delta S \to \partial_S V = v$, i.e. the infinitesimal volume per salinity class is obtained. The local thickness of the finite volume ΔV is denoted as Δn, that for $\Delta S \to 0$ the infinitesimal local thickness per salinity class, $\Delta n/\Delta S \to (\partial_n s)^{-1}$ is obtained.

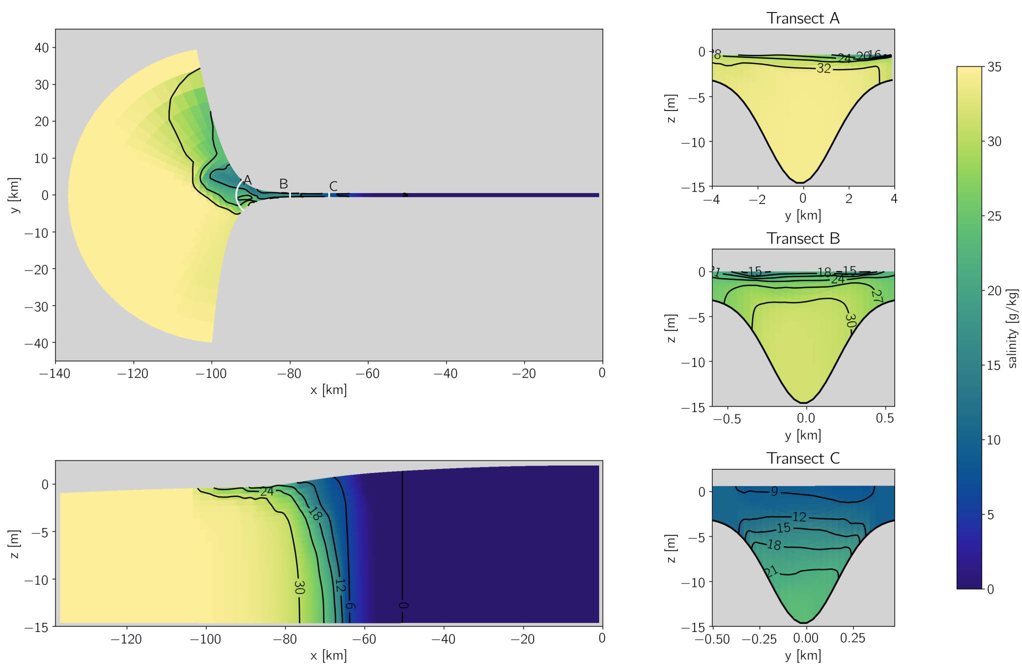

FIG. 4. Idealized convergent estuary model: salinity distribution during high water as gauged at $x = 0$. The upper left panel shows surface salinity, the lower left panel shows a longitudinal transect (at $y = 0$ km), and the right panels show a cross-sectional transect at three different locations (note the different horizontal scales).

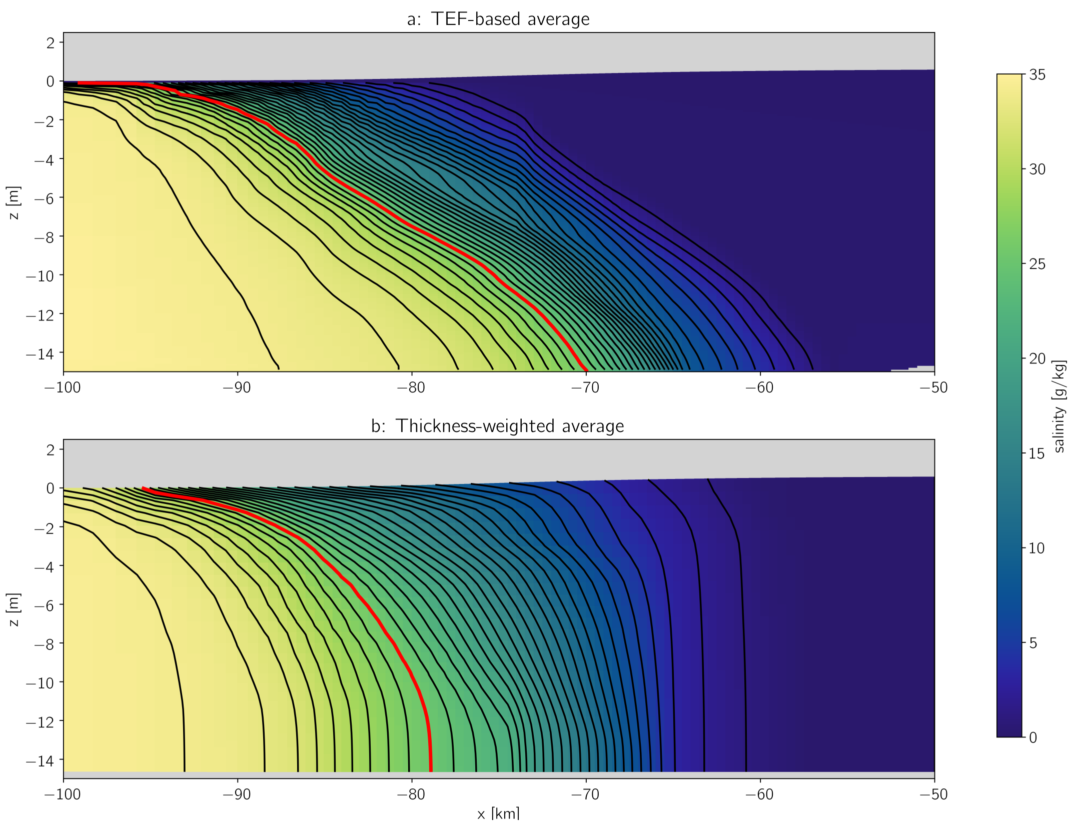

FIG. 5. Idealized convergent estuary model: averaged salinity distribution and isohaline positions at the centerline of the estuary ($y = 0$) resulting from TEF-based (panel a) and thickness-weighted (panel b) averaging. Isohalines are shown in steps of $\Delta S = 1$ g/kg. The red line represents the position of the isohaline with $S = 25$ g/kg.

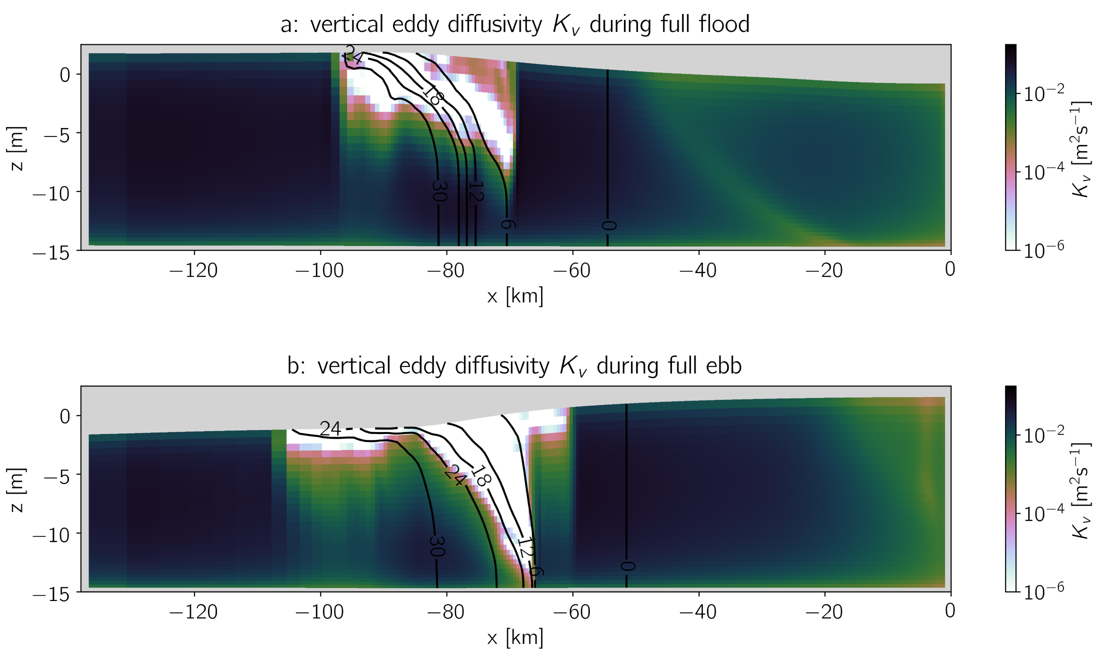

FIG. 6. Idealized convergent estuary model: eddy diffusivity K_v (color code) and salinity s (isolines) during full flood (panel a) and full ebb (panel b) at the centerline of the estuary ($y = 0$).

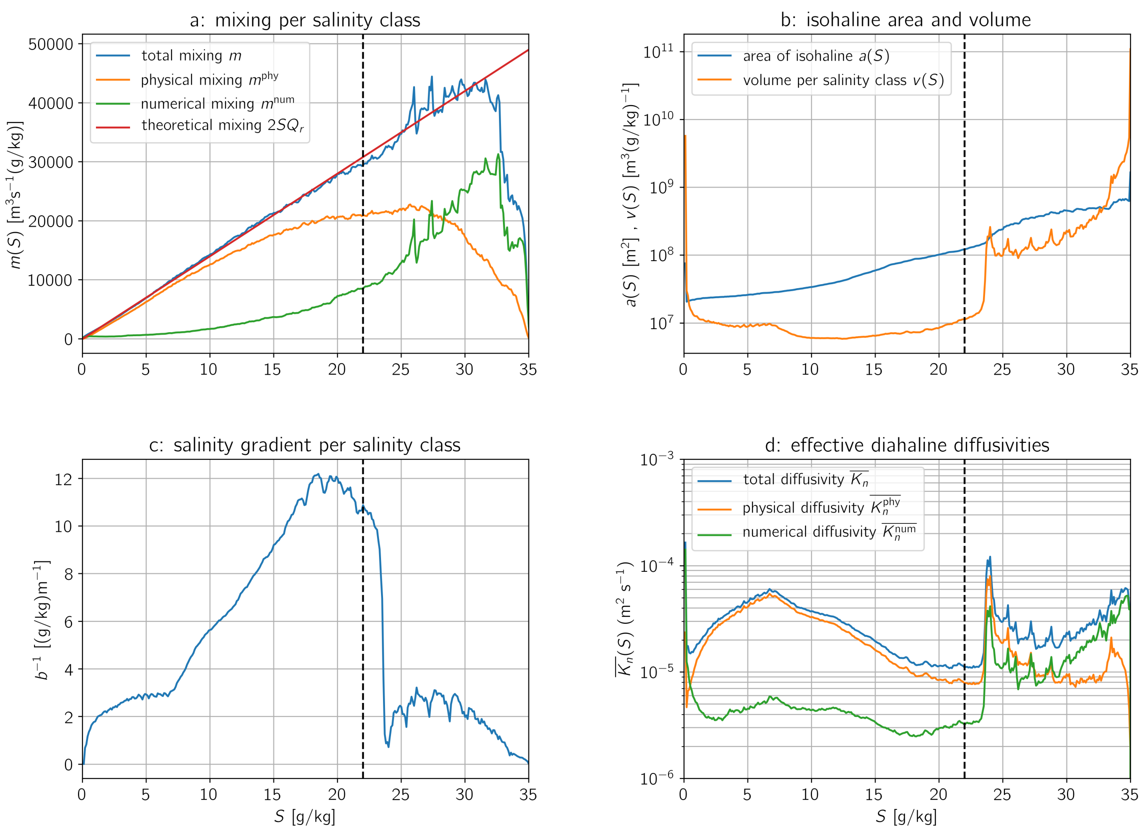

FIG. 7. Idealized convergent estuary model averaged over 10 tidal periods during a quasi-periodic state: properties defining effective diahaline diffusivities as function of salinity. a: physical, numerical and total mixing per salinity class in comparison to the universal law $m(S) = 2SQ_r$; b: area of isohaline S, $a(S)$, and volume per salinity class, $v(S)$; c: resulting averaged salinity gradient, b^{-1}; d: effective physical, numerical and total diahaline diffusivity. The vertical hatched line indicates the minimum salinity which reaches the open boundary.

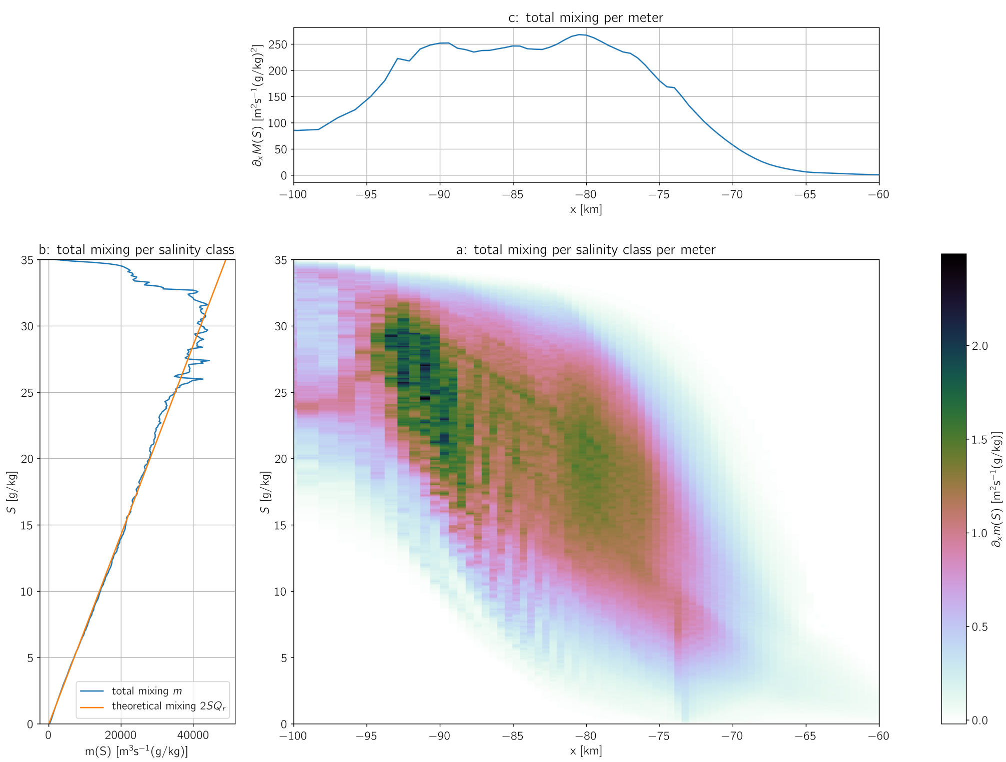

FIG. 8. Idealized convergent estuary model averaged over 10 tidal periods during a quasi-periodic state: mixing per salinity class and longitudinal distance, $\partial_x m(S)$ (panel a), mixing per salinity class, $m(S) = \partial_S M(S)$ (integrated along the estuary, panel b), and mixing per longitudinal distance, $\partial_x M(S)$ (integrated over salinity, panel c).

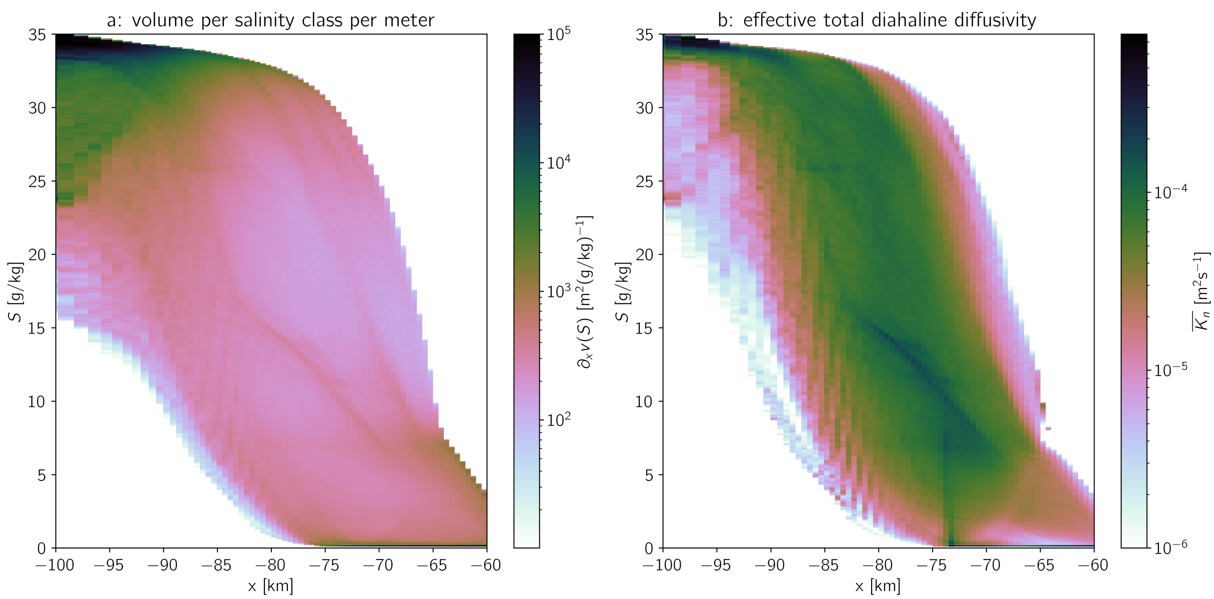

FIG. 9. Idealized convergent estuary model averaged over 10 tidal periods during a quasi-periodic state: volume per salinity class and longitudinal distance, $\partial_x v(S)$ (panel a), and effective total diahaline diffusivity as function of salinity class and longitudinal distance, $\overline{K_n}$ (panel b).

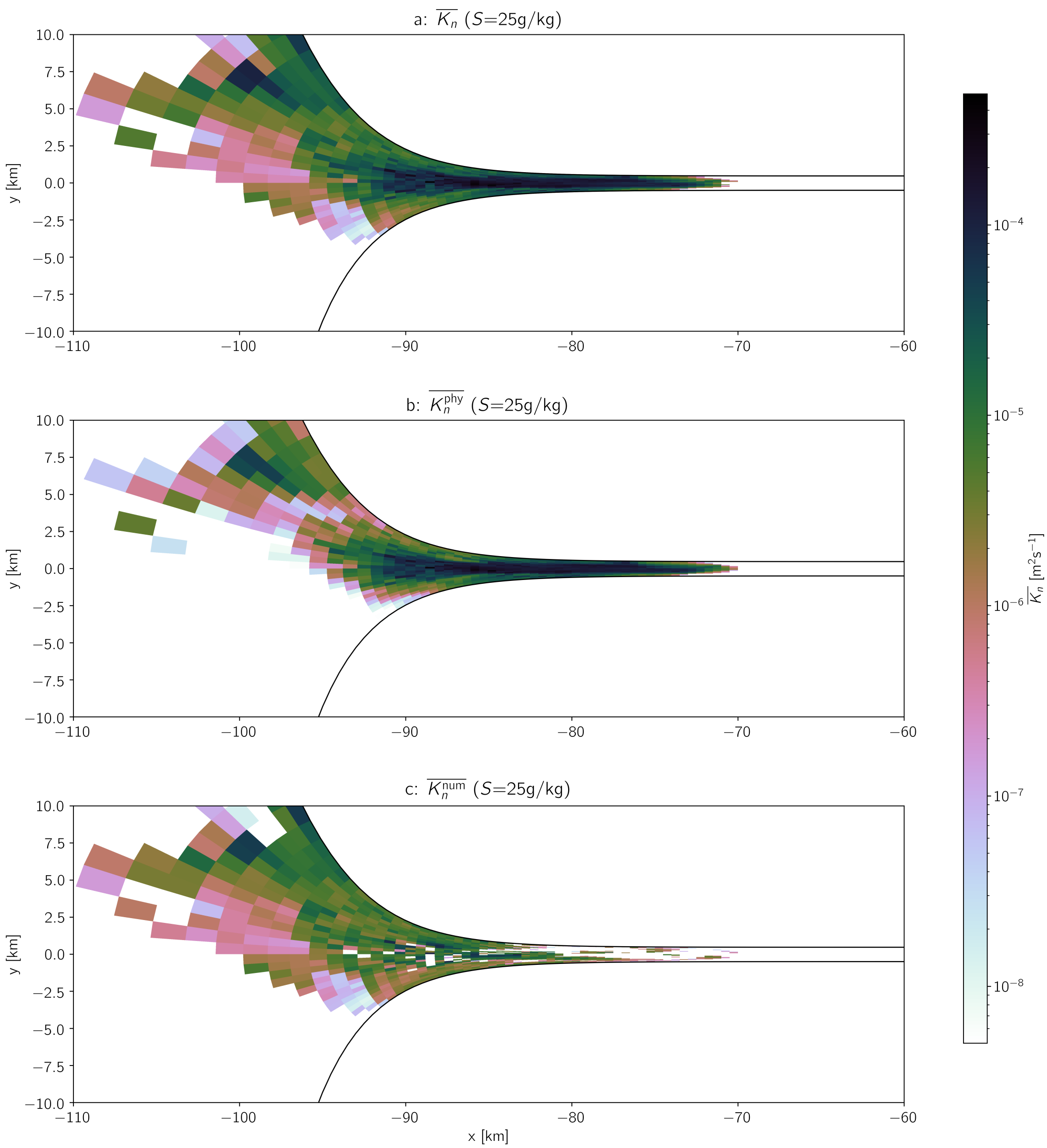

FIG. 10. Idealized convergent estuary model averaged over 10 tidal periods during a quasi-periodic state: total (panel a), physical (panel b) and numerical (panel c) effective diahaline diffusivity across the 25-g/kg-isohaline as function of x and y. Note that the x and the y axes have different scalings.